Illuminating the concentration dependence of charge transfer kinetics in lithium-ion battery blend-electrodes
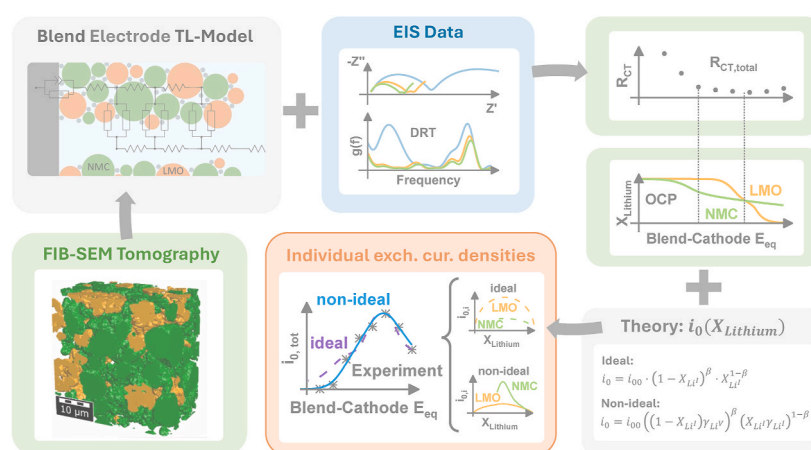
Marc Schiffler [*] ⓘ, Julian Ulrich ⓘ, Adrian Lindner ⓘ, André Weber ⓘ

Institute for Applied Materials, Electrochemical Technologies (IAM-ET), Karlsruhe Institute of Technology, Adenauerring 20b, 76131, Karlsruhe, Germany

HIGHLIGHTS

- Extraction of SoC dependent exchange current density of NMC-LMO blend electrode.
- Comparison of ideal and non-ideal concentration dependent charge transfer kinetics.
- Better agreement with experimental data using non-ideal charge transfer kinetics.

GRAPHICAL ABSTRACT

ARTICLE INFO

ABSTRACT

Blending of different active materials for lithium-ion electrodes offers great opportunities to combine advantageous properties in order to achieve an overall improved cell performance. While electrochemical models for blend electrodes are readily available, the parametrization remains challenging since the contributions of the two or more blend components are difficult to distinguish and material specific and area specific parameters from literature are not always applicable. Here we present a way to directly extract the charge transfer resistance from a blend electrode using impedance spectroscopy, microstructural analysis and transmission line modeling. To differentiate between the contributions of each active material we make use of the concentration dependence of the exchange current density in intercalation electrodes. We apply and compare two theoretical derivations of concentration-dependent charge transfer kinetics to model the behavior of the two active materials. The first is the common Newman formulation and the second is a thermodynamically more consistent, non-ideal approach. When comparing the two approaches to experimental data, we find a better agreement for the non-ideal approach than for the ideal one. These findings encourage further investigations of non-ideal charge transfer formulations which could improve not only blend electrode- but also single material electrode models.

---

* Corresponding author.
  E-mail address: marc.schiffler@kit.edu (M. Schiffler).

1. Introduction

The blending of active materials allows the combination of advantageous properties in order to improve the overall performance of lithium-ion battery electrodes [1]. Synergy effects and internal dynamics in blend electrodes have been studied extensively [2–7]. Liebmann et al. [6] investigated kinetic and thermodynamic properties of blended cathode materials and found that blending does not alter the intrinsic kinetic properties of the active materials. Therefore, the blended electrode behavior can be described as the weighted sum of its individual components. In blend electrodes that are made of active materials showing very different open-circuit potential (OCP) profiles, each active material phase is lithiated or delithiated almost successively, while the material with the higher slope in OCP delithiates slower. This results in significant differences in their respective lithiation degree [4] and consequently different charge transfer resistances, leading to a complex dependency between the overall blend electrode state-of-charge and its apparent exchange current density. Electrochemical models for blend electrodes have been proposed and shown effective [8–10] by using multi particle approaches. However, the accurate parametrization of these models remains challenging. A major hurdle, which equally applies for single active material electrodes, is the availability and comparability of charge transfer parameters in literature. For the parametrization of an electrochemical model the area specific rate constant, commonly expressed in the form of an exchange current density i_0 is needed. Since there is no standardized method established on how to determine the active surface area of a battery electrode, values from literature are hardly comparable [11–13]. Addressing this issue, Costard et al. [14] presented a method to obtain the surface specific exchange current density of different cathode materials combining impedance spectroscopy and focused ion beam - scanning electron microscopy (FIB-SEM) tomography. The extraction of the charge transfer resistance was done with the help of transmission line modeling (TLM) [15–17] which has been applied successfully in previous publications for porous graphite anodes [18] and NMC cathodes [14]. While for single materials this method is solid, it has not been applied to blend electrodes yet and requires further refinement. Firstly, the FIB-SEM segmentation needs to be capable of distinguishing between the two or more active materials present in the blended electrode. Secondly, the impedance response must be modeled correctly and attributed to the respective active materials. The attribution of charge transfer resistance to both active materials is however not directly possible. Therefore, we rely on theory describing the concentration dependent charge transfer resistance for each material as an additional constraint in order to extract the exchange current density of each material.

For this approach, the relation between the lithiation degree (or state of charge (SoC)) and the exchange current density is crucial. In most common lithium-ion battery models it is described by the expression introduced by Newman and coworkers [19,20] in 1993 (later described in Eq. (18)). It assumes ideal kinetics on the one hand, meaning that the activity coefficients in the Nernst equation are assumed to be constant and followingly the activities are proportional to the concentrations. Additionally, it assumes the transfer coefficients to sum up to unity and to be symmetrical ($\alpha_a = \alpha_c = 0.5$). This formulation results in a concentration dependency in the form of a semicircle, where the exchange current density tends towards zero for either fully lithiated or completely empty electrodes and has its maximum at a lithiation degree of 0.5. While this might be an adequate approach for some intercalation materials, there is a lack of experimental evidence proving the solely concentration-based expression to hold true for all types of lithium intercalation electrode materials [11,12,21]. For example, Morasch et al. [21] observed a general U-shape dependency of the charge transfer resistance for NMC111 obtained by impedance spectroscopy. However, they could only reproduce the experimental data by applying a transfer coefficient of $\alpha = 2$ which is not backed by common theoretical

derivations of charge transfer coefficients [20,22]. The impedance results of Moškon and coworkers [23] showed a parabola shaped dependency between the exchange current density and the lithium concentration in NMC622 which also deviates significantly from the Newman expression. In addition to the lack of experimental proof, there are theoretical considerations concerning the general validity of the Newman formulation. One being the inconsistency of using empirical (non-ideal) OCP data on the one hand, and ideal formulations for the exchange current density on the other hand, as first described by Zhang et al. [24]. Based on these inconsistencies, several publications proposed alternative expressions for i_0 using thermodynamically more consistent approaches [25–27]. They however still lack experimental prove.

In this work we make use of two approaches, the ideal (Newman) formulation and a thermodynamically more consistent approach, in order to thoroughly parametrize a commercially available NMC111-LMO blend cathode. We extend the approach presented by Costard et al. [14] by including the identification and separation of the two active material phases using FIB-SEM microstructure reconstruction. The obtained microstructural parameters allow the extraction of surface specific values from impedance measurements and transmission line modeling to accurately quantify the exchange current density. From the measured overall exchange current density, we then obtain the single exchange current densities of each material using reverse analysis based on the lithiation degree and the underlying theory for concentration-dependent charge transfer kinetics.

2. Methods

2.1. Experimental

2.1.1. Preparation of experimental cells

In this work the cathode of a commercial 20Ah pouch cell (ENERTECH SPB58253172) was examined. To extract the electrode sheets the pouch cell was first discharged to 3.0 V and then opened in a glovebox with argon atmosphere. The electrode sheets were washed in dimethyl carbonate (DMC) directly after opening and a second time after punching 18 mm diameter coins for the build of the experimental cell. For the measurements the outer sheets of the cell were used, which are coated single-sided only. The NMC111-LMO cathode was used as the working electrode (d = 18 mm) against lithium foil (MSE PRO™, d = 17.5 mm) as the counter electrode. A 280 µm thick glass fiber separator (VWR® Type 696) was used with 150 µl of 1M LiPF$_6$ in EC:DMC (1:1 v:v) (Sigma-Aldrich) as electrolyte. The experimental cells were assembled within an EL-Cell® PAT-Cell setup. Before the impedance measurements the cells were cycled three times between 3.6 V and 4.3 V with a CCCV profile and a current of 0.5 C using the *BaSyTec CTS-LAB Battery Test System*. To ensure reproducibility three identical cells were built for the impedance measurement. An additional symmetrical cell was built to assist peak identification. For the symmetrical cell two cathodes were cycled to 3.9 V against lithium metal [28] using a CCCV charging scheme and an additional 3 h hold at 3.9 V. Afterwards the two electrodes were extracted, washed in DMC, and then mounted against each other in a new cell case using the same separator and electrolyte configuration as mentioned above.

2.1.2. Impedance spectroscopy

The impedance spectra were measured using a *Solartron analytics 1470E Cell Test System with Scribner Multistat Software*. We used potentiostatic excitation with an amplitude of 5–10 mV in the frequency range from 1 mHz to 1 MHz. The voltage range for the investigation (3.6 V–4.3 V) was chosen according to the operating voltage window of the cathode within the commercial pouch cell from which the cathode was extracted. The voltage levels for impedance spectroscopy were set in 0.1 V steps from 3.6 V to 4.3 V using a CCCV scheme with a current stop condition of I = C/100 for the CV step. An additional CV step of 3 h at the desired voltage level and an additional waiting time of 1 h was added to ensure

full equilibration. All measurements were performed at a temperature of 25 °C in a Vötsch VT 4002 climate chamber. The given voltage values in the results section are the equilibrated open circuit voltages of the cell directly before the impedance measurement. The impedance spectra were analyzed by their distribution of relaxation times (DRT) [29,30]. The validity of the spectra, meaning the linearity, time invariance and causality of the system, was verified by the Kramers-Kronig relation [31].

2.1.3. Electronic conductivity

The effective electrical resistance of the composite electrode was measured using a *HIOKI RM2610 Electrode Resistance Measurement System* [32]. The working principle of this measurement is as follows: a constant current is applied to the surface of the electrode and the potential distribution is obtained using a multipoint potential measurement. A finite volume model is then fitted to the measurement using the composite volume resistivity and the interface resistance as fitting parameters. The thickness of the porous electrode as well as the thickness of the current collector and its conductivity are considered as fixed input parameters in the model fit. Due to the negligible ionic conductivity of the (dry) electrode, the measured conductivity is considered as the effective electronic conductivity of the porous electrode layer $(\sigma_{el,eff})$.

2.1.4. FIB-SEM tomography of blend electrode

To assess the microstructure of the investigated blend electrode we performed two high-resolution FIB-SEM tomographies. This is necessary to fully capture both the carbon-binder-domain (CBD) as well as both active materials while maintaining high image quality.

For the first FIB-SEM tomography, which was intended for the investigation of the CBD, the cathode was prepared by cutting a 5×5 mm^2 sample and subsequent vacuum infiltration with contrast rich silicon-based resin (Elastosil R604B, Wacker Chemie). A thin protective multilayer consisting of two layers of sputtered platinum (EM ACE200, Leica, Germany) separated by drip coated carbon adhesive (M-Bond, Micro Measurements, Germany) was applied to the surface to ensure high milling quality. The so-prepared sample was transferred into Zeiss 1540 XB (Zeiss Microscopy, Germany) equipped with a Ga$^+$-focused-ion-beam (FIB). The slice & view process was performed using a beam current of 2 nA with a slice thickness of 100 nm. Imaging was performed at 1.3 kV acceleration voltage. Roughly 600 images were taken, providing insight into a volume of $45 \times 40 \times 40$ µm^3 with a pixel size of 45 nm.

For the second FIB-SEM tomography, which was intended for the investigation of the active material blend, an epoxy resin (EpoFix, Struers) was used in place of the Elastosil. This prevents the CBD from being visible but vastly increases the contrast between pore space and both active materials in InLens detection mode. The preparation of the protective layer as well as the FIB settings remain unchanged. Exemplary images taken during the tomography are shown in Fig. 1.

2.1.4.1. Image processing and evaluation.
Detailed description of the image processing of CBD structures (tomography 1) in cathode material is outlined elsewhere [33]. To assess the active material distribution of the blend electrode (tomography 2), images of the second tomography were aligned using an algorithm based on Scale-Invariant-Feature-Transform (SIFT) implemented in ImageJ. After cropping a suitable Region-of-Interest (ROI), noise and any remaining milling artifacts were removed by three filter steps: Anisotropic Diffusion Filter, Curtaining Filter and Non-Local Denoising. The curtaining filter is implemented in GeoDict 2024 [34] while the others are part of the Fiji distribution of ImageJ. Finally, segmentation of the two active materials, as well as the homogenized pore/CBD phase was performed by region growing, sometimes referred to as watershed segmentation or Multi-Phase Segmentation. Results of the segmentation and exemplary data are shown in Fig. 1.
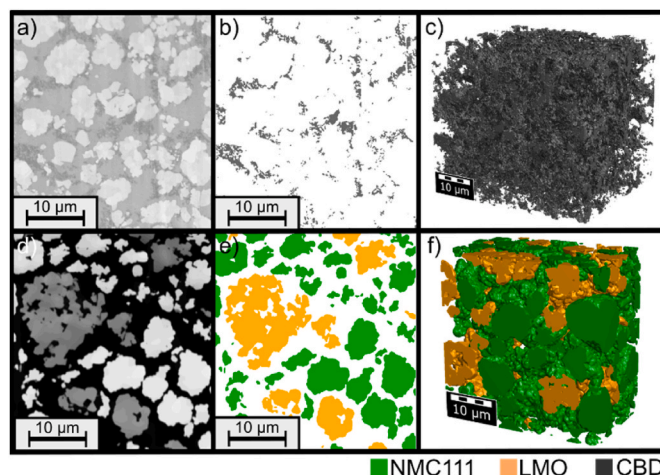

Fig. 1. FIB-SEM Tomography of the NMC111-LMO blend electrode. Tomography 1 (a, b, c) is used to characterize the CBD and calculate pore space tortuosity. Tomography 2 (d, e, f) quantifies active material distribution, volume fractions and surface areas for each active material (NMC111, LMO) individually.

Specific surface areas of the two active materials were calculated using the MatDict module in GeoDict on tomography 2 containing a homogenized pore/CBD phase as well as both active materials segmented individually. The approach is based on the work of Ohser et al. [35] and more detailed information is provided in Ref. [36].

Pore space tortuosity τ was calculated using the DiffuDict module [37] in GeoDict using tomography 1 containing the pore space, CBD as well as an active material phase where NMC111 and LMO are not segmented individually. CBD was considered blocking for the ionic transport. We mention here that the definition of the tortuosity τ used in this work is equivalent to the tortuosity factor in GeoDict and other sources and thus directly representing the impact of the microstructure on the conductivity of the considered phase. The entire approach to image processing and evaluation is in line with previous work [14,33,38].

2.1.5. Energy-dispersive X-ray spectroscopy

Active material stoichiometries were obtained with energy-dispersive X-ray spectroscopy (EDX) on electrode cross-sections after the tomography was performed. Measurements were conducted inside the Zeiss XB 1540 equipped with a Bruker EDX system at accelerations voltages of 20 kV. Spectral data of several measurements was evaluated using Bruker Esprit and aggregated to obtain the stoichiometries of both active materials. Only transition metal signals (manganese, cobalt and nickel) were evaluated quantitatively.

2.1.6. Open circuit potentials (OCP)

For the concentration dependent parametrization of the exchange current density, the open circuit potential (OCP) of each single material along the lithiation degree is a key. The experimental OCPs of the single materials that are used in this work have been taken from literature. In Fig. 4 the experimental OCPs of NMC111 [11] (Fig. 4a, solid line) and LMO [39] (Fig. 4c, solid line) are shown. They are expressed as a function of the lithiation degree. While the measurement of the OCP curve is done by cycling at very small C-rates or by applying small current pulses, relating the voltage to the precise lithium content is challenging. After cycling at a rate of C/100 Schmalstieg et al. [11] held the NMC111 electrode at two voltage levels (3.0 V and 4.2 V) for several hours and then performed ICP-OES measurements on the extracted electrodes to determine the ratio between lithium and the NMC111 host material. With these two points the lithiation degree over the whole OCP range could be determined. For LMO, the OCP and its respective

lithiation degree available in literature show large variations [10,40, 41]. In this work we used the OCP-curve of a pure LMO electrode [39] cycled at a low rate (C/40). We assumed the lithiation degree to be close to zero at the steep increase towards 4.5 V and related the drop-off at 3.8 V with a lithiation degree of around 1.

2.2. Modeling

2.2.1. Transmission line model for blend electrode

To accurately model and extract the exchange current density from the impedance measurements, a transmission line model [15,16] was used. The transmission line model is an equivalent circuit model that describes the impedance Z_{TLM} of a porous electrode including the electronic path χ_{el} through the active material and conductive binder phase and an ionic path χ_{ion} through the electrolyte filled pores of the electrode (see also Fig. 2).

$$Z_{TLM}\,[\Omega] = \frac{\chi_{ion}\chi_{el}}{\chi_{ion}+\chi_{el}}\left(L+\frac{2\kappa}{sinh\left(\frac{L}{\kappa}\right)}\right)+\kappa\frac{\chi_{ion}^2+\chi_{el}^2}{\chi_{ion}+\chi_{el}}coth\left(\frac{L}{\kappa}\right) \tag{1}$$

$$\kappa\,[m]=\sqrt{\frac{\xi}{\chi_{ion}+\chi_{el}}} \tag{2}$$

When L is the thickness of the electrode then the ionic χ_{ion} and electronic χ_{el} length specific resistances are given as

$$\chi_{ion}\left[\frac{\Omega}{m}\right]=\frac{R_{ion}}{L}=\frac{1}{\sigma_{ion}}\cdot\frac{1}{A}\frac{\tau}{\varepsilon} \tag{3}$$

$$\chi_{el}\left[\frac{\Omega}{m}\right]=\frac{R_{el}}{L}=\frac{1}{\sigma_{el,eff}}\cdot\frac{1}{A} \tag{4}$$

The effective ionic conductivity can be calculated by the tortuosity τ and porosity ε obtained by microstructure characterization and the bulk conductivity σ_{ion} of the electrolyte. Theoretically, the electronic
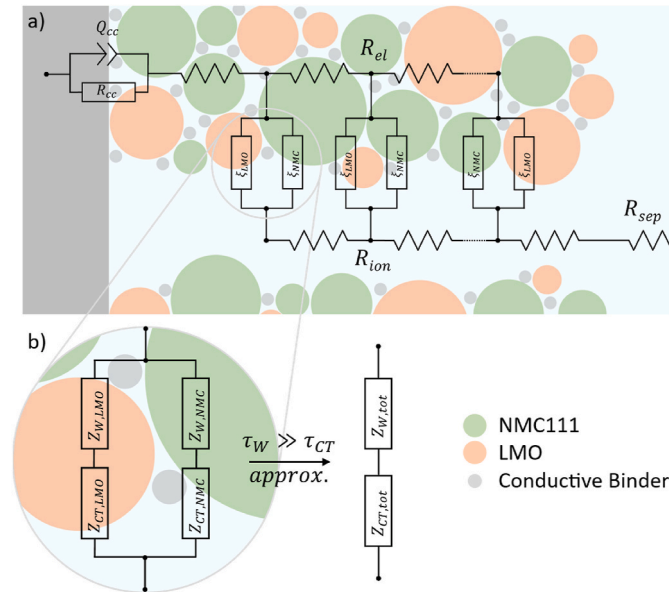

Fig. 2. Transmission Line Model of the NMC111-LMO blend cathode (a). R_{el} is the effective electrical conductivity of the porous electrode which is composed of the electrical conductivity of each active material and the conductive binder domain. Each interface process ξ_i is represented by a charge transfer process $Z_{CT,i}$ and a diffusion process $Z_{FLW,i}$. Since they are connected in parallel, they appear in the impedance spectrum as one charge transfer process $Z_{CT,tot}$ and one diffusion process $Z_{FLW,tot}$ (b).

conductivity $\sigma_{el,eff}$ could also be calculated from the microstructure parameters and the bulk conductivities of each of the different material phases, however as an accurate separation of binder and carbon black is challenging, the calculation is more error prone. Therefore, in this work the effective electrical conductivity of the porous composite layer has been measured directly (see 2.1.3). The interface process ξ (5) includes the charge transfer Z_{CT} modeled by an RQ element (6) and the solid-state diffusion Z_{FLW} modeled by a finite length Warburg element (7).

$$\xi[\Omega m] = (Z_{CT}+Z_{FLW})\cdot L \tag{5}$$

$$Z_{CT}=\frac{R_{CT}}{1+(j\omega)^n Q_{CT}R_{CT}} \tag{6}$$

$$Z_{FLW}=R_{FLW}\cdot\frac{\tanh\left((j\omega\tau)^n\right)}{(j\omega\tau)^n} \tag{7}$$

In Fig. 2 the adapted transmission line model for a blend electrode is shown. In contrast to a single material transmission line model [14], the interface process ξ is represented by two processes ξ_i for each active material in parallel. Each is representing the charge transfer characteristics of one of the two blend materials. However, due to the parallel connection, the two interface processes appear as one single charge transfer process $Z_{CT,tot}$ in the impedance spectrum. To explain this, the parallel connection of a charge transfer process represented by an RC element is given in eq. (8). After reformulation, the total impedance can be written in the form of a single RC element by replacing the individual resistance and capacitance by a total value, as shown in eq. (9). This means that even if the time constants $\tau_i = R_{CT,i}\cdot C_{CT,i}$ of the different active materials differ, the impedance of the blend electrode will exhibit a single time constant $\tau_{tot} = R_{CT,tot}\cdot C_{CT,tot}$. Thus, it is not directly possible to distinguish the contributions of the different blend components in an impedance spectrum or a DRT (see also Fig. 5).

$$\frac{1}{Z_{CT,tot}}=\frac{1}{R_{CT,NMC}}+\frac{1}{R_{CT,LMO}}+i\omega C_{CT,NMC}+i\omega C_{CT,LMO} \tag{8}$$

$$Z_{CT,tot}=\frac{\frac{R_{CT,NMC}R_{CT,LMO}}{R_{CT,NMC}+R_{CT,LMO}}}{1+i\omega\left(C_{CT,NMC}+C_{CT,LMO}\right)\frac{R_{CT,NMC}R_{CT,LMO}}{R_{CT,NMC}+R_{CT,LMO}}}=\frac{R_{CT,tot}}{1+i\omega C_{CT,tot}R_{CT,tot}} \tag{9}$$

If the charge transfer resistance $R_{CT,i}$ of each material is known, the total charge transfer resistance can be calculated by eq. (8). In contrast, to determine each single charge transfer resistance from the impedance spectrum of the blend electrode, further constraints are necessary. Therefore, we apply a reverse analysis approach adding an additional constraint by relying on the theory for concentration-dependent charge transfer kinetics of insertion electrodes, which will be explained in more detail in the next chapter. Since our focus is the charge transfer resistance, we don't attempt to extract the two different diffusion processes involved. As the time constants of the diffusion processes are usually much higher than those of the charge transfer processes, we can approximate the parallel connection of the two materials as one series connection of one total charge transfer and one total diffusion resistance, as shown in Fig. 2.

In Fig. 3 the full equivalent circuit model (ECM) for the cathode and the lithium foil counter electrode, as applied for fitting of impedance spectra is shown. In addition to the transmission line model representing the porous cathode, one RQ-element represents the charge transfer process at the surface of the lithium foil counter electrode and another RQ-element represents the contact resistance between active material and current collector of the cathode. Finally, the losses in the electrolyte along the separator and other ohmic losses in the setup are represented by an ohmic resistor.

2.2.2. Exchange current density

The Butler-Volmer equation (10) describes the reaction rate expressed as a current density, which depends on the surface
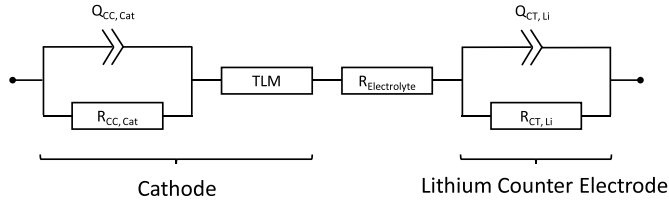
Fig. 3. Equivalent circuit model (ECM) of the cell under test. The charge transfer of the lithium counter electrode as well as the contact resistance is modeled by an RQ element. The porous cathode is modeled by a transmission line model (see Fig. 2). The Electrolyte resistance is represented by an ohmic resistance.

overpotential between electrode and bulk electrolyte.

$$i_{CT} = i_0 \left[\exp\left((1-\alpha) \cdot \frac{F\eta_{CT}}{RT} \right) - \exp\left((-\alpha) \cdot \frac{F\eta_{CT}}{RT} \right) \right] \quad (10)$$

Where i_{CT} is the charge transfer current depending on the overpotential η_{CT}. i_0 is the exchange current density, α the charge transfer coefficient, F the Faraday constant, R the universal gas constant and T the temperature. The exchange current density i_0 can be obtained from impedance spectroscopy. For small overpotentials and currents, as it is the case in EIS, the equation can be linearized as follows:

$$i_{CT} = i_0 \cdot \frac{F\eta_{CT}}{RT} \quad (11)$$

From this the area specific charge transfer resistance $r_{CT}[\Omega m^2]$ can be calculated. It should be noted that r_{CT} and i_0 are expressed with respect to the active (accessible) surface area of the active material particles in the electrode layer.

$$r_{CT} = \frac{\eta_{CT}}{i_{CT}} = \frac{1}{i_0} \cdot \frac{RT}{F} \quad (12)$$

If the active surface area A_{act} of the sample is known and the charge transfer resistance R_{CT} is obtained from impedance spectroscopy, i_0 can be calculated as follows:

$$i_0 = \frac{1}{R_{CT}A_{act}} \cdot \frac{RT}{F} \quad (13)$$

For an intercalation electrode the exchange current density i_0 is dependent on the lithiation degree which is defined by the actual lithium concentration in the active material phase divided by the maximum concentration: $X_{Li^I} = c_s/c_{s,max}$. Any impact of Li-concentration changes in the electrolyte can be neglected as electrolyte diffusion processes, which might create a change of the lithium concentration at the active material surface in the electrode, are negligible at small amplitudes and exhibit much larger time constants [42] and thus do not affect the evaluation of the charge transfer resistance by impedance spectroscopy. By taking into account the parallel connection of the two charge transfer processes introduced in Fig. 2 we can write the total exchange current density as follows:

$$i_{0,tot}(E_{eq}) = \frac{A_{act,NMC}}{A_{act,tot}} \cdot i_{0,NMC}(X_{Li^I,NMC}(E_{eq})) + \frac{A_{act,LMO}}{A_{act,tot}} \cdot i_{0,LMO}(X_{Li^I,LMO}(E_{eq})) \quad (14)$$

Here the total exchange current density $i_{0,tot}(E_{eq})$ is a function of the equilibrium potential of the blend electrode. The exchange current densities of the two active materials $i_{0,NMC}$ and $i_{0,LMO}$ are a function of their respective lithiation degree which itself is a function of the equilibrium potential of the blend electrode E_{eq} as shown in Fig. 6. $A_{act,i}$ is the active material surface of each active material separately (NMC, LMO) and the total active material surface (tot). The individual contributions of $i_{0,NMC}$ and $i_{0,LMO}$ can be obtained iteratively so that eq. (14) describes the experimental $i_{0,tot}$ as good as possible.

2.2.2.1. Concentration dependence of charge transfer in intercalation electrodes. The Lithium intercalation reaction can be described by the following chemical reaction:

$$Li^+ + Li^V + e^- \rightarrow Li^I \quad (15)$$

Here, Li^+ is the lithium-ion in the electrolyte phase, Li^V is a vacancy in the host material, and Li^I is intercalated lithium in the host material. The expression for the concentration-dependent exchange current density is
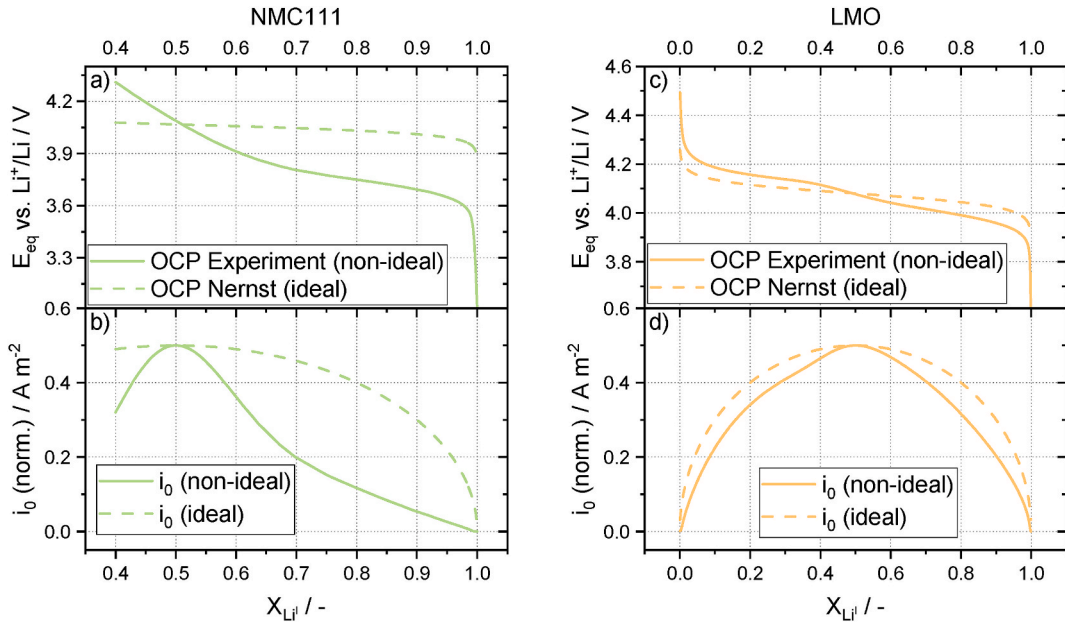

Fig. 4. Open circuit potential of (a) NMC111 [11] and (c) LMO [39] from experiments (solid lines) and ideal OCP (dashed lines) calculated by the ideal Nernst (eq. (20)) with constant activity coefficients. Normalized exchange current densities of (b) NMC111 and (d) LMO over lithiation degree using the non-ideal approach (eq. (19)-(21)) (solid lines) and the ideal approach (eq. (18)) (dashed lines).
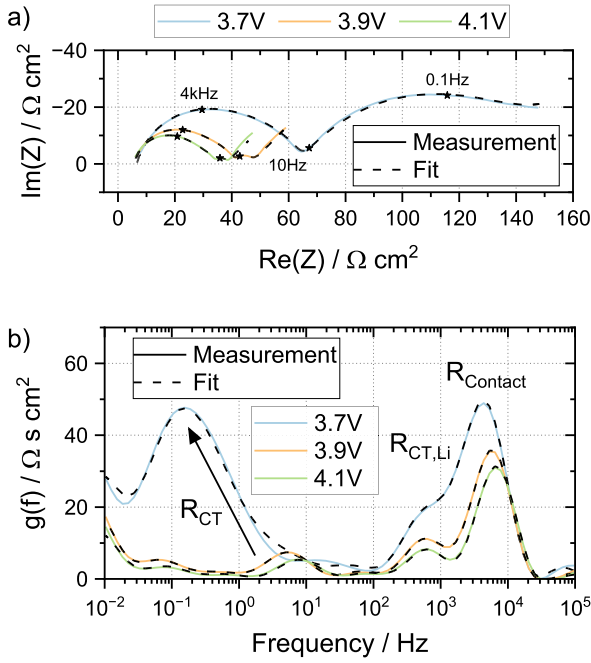
Fig. 5. Impedance spectra of NMC111-LMO blend electrode at three representative OCPs vs. Li$^+$/Li. (a) Nyquist representation: The first semicircle is a combination of the contact resistance of the cathode and the charge transfer resistance of the lithium foil counter electrode. The second semicircle is the charge transfer resistance of the blend cathode. (b) Distribution of relaxation times for detailed peak identification: R_{CT} being the combined charge transfer resistance of the blend cathode, $R_{CT,Li}$ the charge transfer resistance of the lithium foil counter electrode and $R_{Contact}$ the contact resistance of the cathode.
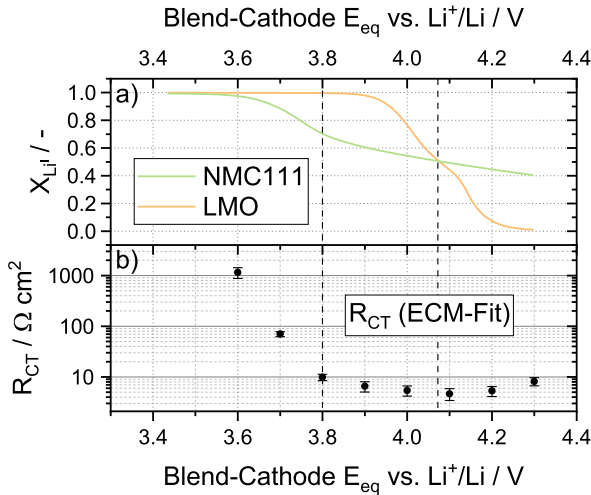

Fig. 6. Combined plot of (a) Lithiation degree of NMC111 [11] and LMO [39] and (b) the measured charge transfer resistance from impedance spectroscopy and ECM-fit plotted over the overall blend-cathode open circuit potential. The error bars in (b) represent the mean value and standard deviation of three individual experimental cells.

obtained by deriving the Butler-Volmer equation from transition state theory as presented in Ref. [43]. By assuming electron activity to be negligible ($a_e = 1$) and applying it to equation (15) we obtain the following expression:

$$i_0 = \frac{\kappa \cdot k_B T}{h \gamma^\ddagger} \left(a_{Li^v} a_{Li^+}\right)^\beta a_{Li^l}^{1-\beta} \tag{16}$$

where k_B is the Boltzmann constant, h the Planck constant, T the temperature, κ a proportionality constant and $\gamma^\ddagger$ the activity coefficient of the transition state. The activities a_i can be written in terms of the species concentration c_i and the activity coefficient γ_i as follows:

$$a_i = \frac{c_i}{c_{i,ref}} \cdot \gamma_i \tag{17}$$

If we take the maximum lithium concentration in the active material as the reference concentration, the activities in the solid phase can be expressed with respect to the lithiation degree $X_{Li^l} = c_{Li^l}/c_{Li^l,max}$ and $X_{Li^v} = 1 - X_{Li^l}$. For the ideal (Newman) case it is assumed, that the activity coefficients of the intercalated Lithium and the vacancies in the active material as well as the activity coefficient of the transition state are constant, which makes the activity solely a function of the concentration. During EIS the electrolyte activity is constant as well and is not expected to change with SoC. Followingly, it can be combined with the pre-factors to a standard exchange current density i_{00}, which leads to the formulation proposed by Newman and coworkers [19,20] (see eq. (18)).

$$i_0 = i_{00} \cdot (1 - X_{Li^l})^\beta \cdot X_{Li^l}^{1-\beta} \tag{18}$$

For the transfer coefficient $\beta = 0.5$ is assumed. The expression results in a semicircle for the exchange current density over its lithiation degree (see Fig. 4(b–d), dashed lines). However, as shown in recent publications [26,27], for electrochemical reactions the concentration dependence of the exchange current density might be better described using non-ideal activities. Therefore, we also apply a non-ideal approach in which we consider only the activity coefficient of the transition state to be constant. This leads to the following formulation of the exchange current density:

$$i_0 = i_{00} \left((1 - X_{Li^l}) \gamma_{Li^v}\right)^\beta (X_{Li^l} \gamma_{Li^l})^{1-\beta} \tag{19}$$

In order to calculate the activity coefficients in a thermodynamically consistent way we take the OCPs of each material into account. We adopt the formulation of the Nernst equation proposed by Colclasure et al. [26] for lithium intercalation electrodes (see eq. (20)), where ΔG° is the Gibbs-Free Energy under standard conditions ($X_{Li^l} = 0.5$). X_{Li^l} is the mole fraction of intercalated lithium $X_{Li^l} = c_{Li^l}/c_{Li^l,max}$ and γ_{Li^l} is the activity coefficient for intercalated lithium and γ_{Li^v} the activity coefficient of a lithium vacancy.

$$E_{ref}^{eq} = \frac{\Delta G^\circ}{F} + \frac{RT}{F} \ln \left(\frac{(1 - X_{Li^l}) \gamma_{Li^v}}{X_{Li^l} \gamma_{Li^l}}\right) \tag{20}$$

The relation between the activity coefficients of vacancies and intercalated lithium is given by the Gibbs-Duhem equation for binary mixtures [27]:

$$X_{Li^l} \cdot \frac{d \ln \gamma_{Li^l}}{d X_{Li^l}} = (1 - X_{Li^l}) \cdot \frac{d \ln \gamma_{Li^v}}{d X_{Li^v}} \tag{21}$$

The experimental OCP curves are then used to calculate the activity coefficients with respect to the intercalation fraction. To do so, we introduce the condition that the Potential E_{ref}^{eq} in eq. (20) must equal the measured OCP. Values between the measured points are interpolated linearly. This algebraic condition is solved alongside the differential equation in (21) using an implicit DAE (Differential-Algebraic Equation) solver in MATLAB® (ode15i).

3. Results & discussion

The results of the FIB/SEM reconstruction as well as all further parameters used in the model are listed in the appendix (Table 1).

3.1. Ideal vs. non-ideal exchange current density

In Fig. 4 (a, c) (solid lines), the experimental open circuit potentials (OCPs) of NMC111 [11] and LMO [39] are shown. Additionally, the

ideal OCP calculated by the Nernst equation with ($\gamma_i = const$) is shown in Fig. 4 (a, c) (dashed lines). In Fig. 4 (b, d) the normalized ideal exchange current density calculated by eq. (18) (dashed lines) and the non-ideal exchange current density calculated by eq. (19) to (21) (solid lines) are shown for NMC111 (b) and LMO (d). All parameters used for the calculations can be found in the appendix (Table 1).

Fig. 4 illustrates the difference between the ideal and non-ideal approach for the calculation of the exchange current density. While for NMC111 the resulting exchange current density differs strongly between the one calculated by the ideal approach and the one calculated by the non-ideal approach, for LMO both approaches lead to an exchange current density that is similar to each other. The main reason for this is the difference in the experimental open circuit potential from which i_0 is calculated. As mentioned before, in most Li-ion battery models the ideal approach is used to calculated the exchange current density over the lithiation degree, which is questionable for some materials as shown above and has been already addressed in Refs. [26,27]. Therefore, we apply and compare both approaches to calculate the exchange current density of the NMC111 and LMO fraction in our blend electrode (see also Fig. 7).

Impedance spectra and related fitting results are shown in Fig. 5 as Nyquist plots (a) and corresponding DRTs (b). Three representative spectra for three open circuit potentials (3.7 V, 3.9 V and 4.1 V) are shown. All spectra ranging from 3.6 V to 4.3 V can be found in the supporting information (Fig. S2 and S3). The solid-colored lines are the measured spectra, and the dashed black lines are the respective ECM-fit results. For all voltage levels the DRT shows two peaks in the higher frequency range (800 Hz–10 kHz) and one in the lower frequency range around 10 Hz, shifting towards lower values (<0.1 Hz) for lower voltage levels. Since the spectra were obtained using an experimental cell with a

lithium foil counter electrode the processes had to be carefully separated. For the correct peak identification, an additional symmetric cell (see Fig. S1 in the supporting information) was built for comparison. This allowed us to identify the peak at around 500 Hz as the lithium charge transfer which is only present in the spectra of the cell with the lithium counter electrode. The peak at around 10 kHz was identified as the contact resistance of the cathode, since it is present in both the symmetrical and the half cell. The peak at 10 Hz (at 4.1 V) could then be identified as the main peak of the TLM dominated by the charge transfer in the cathode. This attribution agrees with the strong dependence of the cathode charge transfer on the OCP. We also see a change of the lithium charge transfer and contact resistance which is not straight forward since the charge transfer resistance of the lithium metal is not dependent on the SoC. The explanation for the decrease of lithium charge transfer resistance is the increase of active surface area during the deposition of lithium on the lithium foil during cycling of the cell, resulting in a change of charge transfer resistance. This interpretation is supported by the observation that the characteristic frequency of the Lithium peak is not changing significantly with the change in SoC. It indicates a simultaneous decrease in the charge transfer resistance and an increase in double layer capacitance due to the change of the active surface area (see also eq. (22)).

$$f_R = \frac{1}{2\pi R_{ct} C_{ct}} \quad with \quad R_{ct} \propto \frac{1}{A_{act}} \quad and \quad C_{ct} \propto A_{act} \tag{22}$$

For a better interpretation of the results, the lithiation degrees of both materials are plotted along the voltage of the blend electrode vs. Li$^+$/Li (Fig. 6 (a)). The equilibrated OCP in both materials is the same at any point due to the electrical connection between the particles. This allows us to determine the relation between the potential of the blend
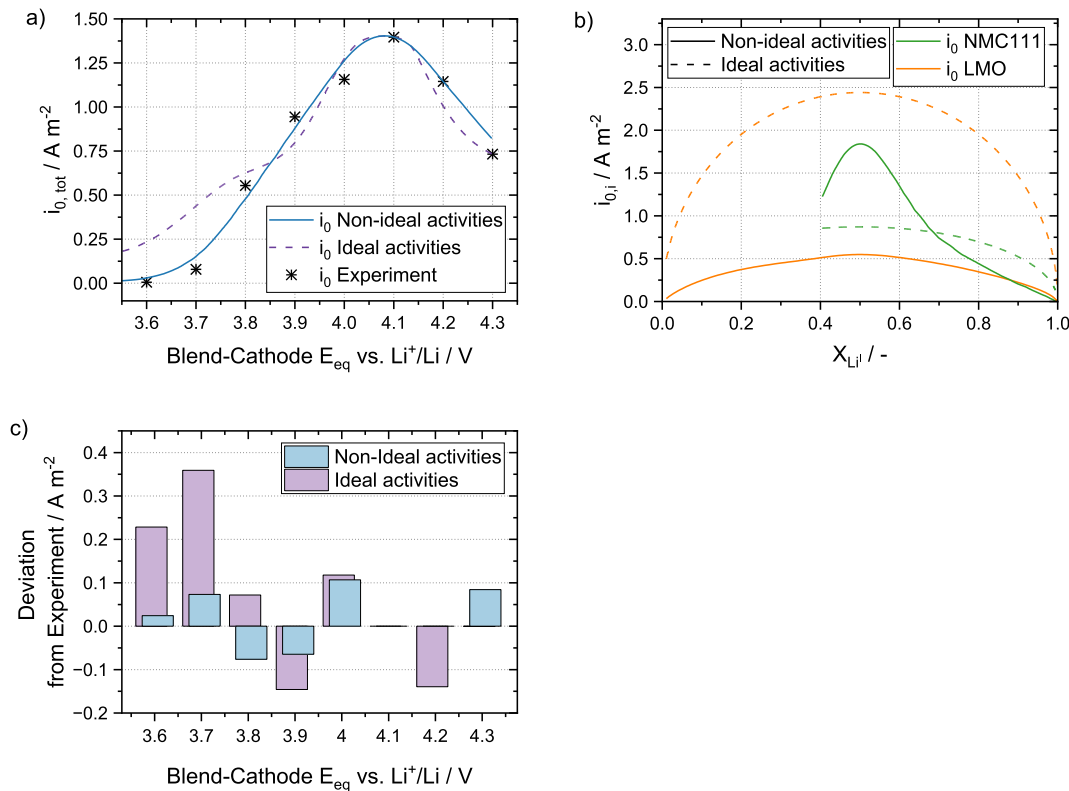

Fig. 7. (a) Total exchange current density from experiment (asterisk) and fitted total exchange current density using the ideal formulation (according to eq. (18), purple) and non-ideal formulation (according to eq. (19)) for the lithiation degree dependent exchange current density. The total exchange current density is the sum of the individual exchange current densities shown in (b). They are obtained by fitting the sum of the individual current densities to the total measured value of i_0 while following the two approaches of concentration dependent charge transfer mentioned above. (c) Deviation of the final values of the total exchange current density from experimental data, for the ideal formulation (purple) and the non-ideal formulation (blue). (For interpretation of the references to color in this figure legend, the reader is referred to the Web version of this article.)

cathode and the lithiation degree in each active material. Together with the lithiation degree of the two materials, the results of the extracted charge transfer resistances from the ECM-fit are plotted in Fig. 6 (b). We can see a minimum of the charge transfer resistance at around 4.1 V where both materials have a lithiation degree of close to 0.5. This agrees with most theories predicting the highest exchange current densities at a lithiation degree of 0.5 and therefore smallest charge transfer resistance. Below 3.8 V we see a steep increase in the charge transfer resistance. At this point the LMO part of the electrode is nearly fully lithiated while the NMC111 part of the electrode is only at a lithiation degree of around 0.7. The steep increase of charge transfer resistance below 3.8 V can be related to the practically fully lithiated and therefore nearly inactive LMO part of the electrode on the one hand and on the other hand to an accelerated increase in charge transfer resistance of the NMC111 part in this OCP range.

To determine the contribution of each single material we apply the expressions for concentration dependent exchange current density presented before (see eq. (18) and (19)). By applying eq. (14) we iteratively determine the values of $i_{00,i}$ for the two active materials so that the mean average error between the calculated $i_{0,tot}$ and the $i_{0,tot}$ obtained from experiment gets minimal. This is done once for the ideal approach (see Fig. 7, dashed lines) and once for the non-ideal approach (see Fig. 7, solid lines). We can see that both approaches can well reproduce the experimental results in the medium to high voltage range $(3.8\,V < E_{eq} < 4.3\,V)$. In the lower voltage range $(E_{eq} < 3.8\,V)$, however, the values of the non-ideal approach are noticeably closer to the experiment. In general, the result of the non-ideal approach agrees better with the experiment (see Fig. 7 (c)) with a mean absolute error of $0.05\,A\,m^{-2}$ for the non-ideal approach and a mean absolute error of $0.13\,A\,m^{-2}$ for the ideal approach. This higher correlation with experimental data for the non-ideal approach allows the statement, that the non-ideal approach is better suited to describe the concentration dependent exchange current density over the lithiation degree for both materials.

In Fig. 7 (b) the resulting values of i_0 vs. X_{Li^i} for each active material are shown. The corresponding data for the non-ideal approach can be found in Table S1 in the supporting information. We can see the characteristic semicircle shape for both materials when using ideal activities (dashed lines). The exchange current densities obtained via the non-ideal activities approach (solid lines) show significant differences in their shapes and absolute values. While for the non-ideal approach the values of the exchange current density for NMC111 are mostly larger than for LMO, it is the opposite for the ideal approach. This shows how dependent the presented method is on the underlying theory for the concentration dependent exchange current density. It also shows how big of an effect the choice of the theory for the exchange current density has, when parametrizing an electrochemical model. While for the total exchange current density at open-circuit potential the difference might not seem that large, in an electrochemical model the two approaches will have a significant effect on the distribution of current densities between the two materials while cycling, especially at higher C-rates. Local and temporal concentration differences at higher C-rates can be quite large in blend electrodes and with that the local overpotentials for each material. The concentration dependency as well as the absolute values for the exchange current density for each material can therefore influence the shape of the charge or discharge curve in a more profound way than it is the case for single material electrodes. Another point we should address is the lower exchange current density for LMO when using the non-ideal approach. This outcome stands in contrast with the generally good rate capability of LMO reported in literature. However, when looking at the rate capability in general, also the diffusion process must be considered. Here, LMO is prone to show significantly lower diffusion resistance than NMC due to its olivine structure. The olivine structure allows three-dimensional diffusion pathways and therefore very good diffusion properties and therefore increased rate capability.

While this work does not attempt to make a final statement about the general validity of the presented ideal and non-ideal approach for concentration dependent charge transfer kinetics, the increased accuracy of the non-ideal approach, especially in the lower voltage region is noticeable. We therefore suggest the non-ideal approach to better describe the charge transfer kinetics of insertion electrodes which also applies for single material electrodes. As mentioned before, this is also backed by experimental results presented in previous works on single material NMC111 electrodes [21,23], which could not be reproduced by using the ideal (Newman) approach. We encourage further studies that directly compare experimental data of single material electrodes with the non-ideal charge transfer theory presented here, in order to proof its general validity.

4. Conclusion

A new approach of determining the concentration-dependent exchange current densities for a lithium-Ion NMC111-LMO blend electrode was presented. Our results rely on the use of several experimental methods including FIB-SEM tomography and EDX measurements to determine the material composition within the blend electrode and its microstructural parameters including the porosity, tortuosity, and the specific active surface area for each of the two materials. Electrochemical impedance spectra of the blend electrode were measured and interpreted. The correct identification and separation of the processes within the experimental cells were assisted by the distribution of relaxation times. The combined charge transfer resistance was extracted from the impedance spectra via transmission line modeling. From the combined charge transfer resistance, the exchange current density of each of the two materials was calculated using reverse analysis. This method relies on the different OCP characteristics of the two blend components in combination with the underlying theory for the charge transfer kinetics. Two approaches for the description of concentration-dependent charge transfer kinetics were compared, one being the ideal concentration dependence, originally developed by Newman and coworkers and a non-ideal approach relying on non-ideal activities. In this context we are the first to directly compare experimental data with a non-ideal charge transfer formulation. We found that ideal kinetics only poorly model the exchange current density in the lower voltage range of the blend-electrode. The results in general favor the use of non-ideal concentration-dependent charge transfer kinetics. Therefore, we highly encourage further investigations of non-ideal formulations of the exchange current density in order to describe the charge transfer in lithium-ion battery electrodes with higher accuracy over the whole operating range.

CRediT authorship contribution statement

Marc Schiffler: Writing – original draft, Visualization, Software, Methodology, Investigation, Conceptualization. **Julian Ulrich:** Writing – review & editing, Software, Methodology, Investigation. **Adrian Lindner:** Writing – review & editing, Visualization, Investigation. **André Weber:** Writing – review & editing, Supervision, Project administration, Funding acquisition.

Declaration of competing interest

The authors declare that they have no known competing financial interests or personal relationships that could have appeared to influence the work reported in this paper.

Appendix A. Supplementary data

Supplementary data to this article can be found online at https://doi.org/10.1016/j.jpowsour.2025.237496.

Appendix

Table 1
List of model parameters

Parameter	Symbol	Value	Unit	Source
Electrodes thickness	L	62	μm	measured
Porosity	ε	0.38	–	FIB/SEM
Tortuosity	τ	2.42	–	FIB/SEM
Specific surface area NMC	$a_{spec,NMC}$	0.50	μm^{-1}	FIB/SEM
Specific surface area LMO	$a_{spec,LMO}$	0.26	μm^{-1}	FIB/SEM
Effective electronic conductivity	$\sigma_{el,eff}$	4	$S\,m^{-1}$	measured[a]
Ionic conductivity electrolyte	σ_{ion}	1.18	$S\,m^{-1}$	[44]
Gibbs free energy of lithium intercalation into NMC	$\Delta G^\circ_{int,NMC}$	393.5	$kJ\,mol^{-1}$	assumed[b]
Gibbs free energy of lithium intercalation into LMO	$\Delta G^\circ_{int,LMO}$	392.4	$kJ\,mol^{-1}$	assumed[b]

[a] HIOKI RM2610 Electrode Resistance Measurement System [32].
[b] Assumed based on measured open-circuit potential at lithiation degree of $X_{Li^i} = 0.5$.

Data availability

Data will be made available on request.

References

[1] Z. Mao, M. Farkhondeh, M. Pritzker, M. Fowler, Z. Chen, Dynamics of a blended lithium-ion battery electrode during galvanostatic intermittent titration technique, Electrochim. Acta 222 (2016) 1741–1750, https://doi.org/10.1016/j.electacta.2016.11.169.

[2] C. Heubner, T. Liebmann, M. Schneider, A. Michaelis, Recent insights into the electrochemical behavior of blended lithium insertion cathodes: a review, Electrochim. Acta 269 (2018) 745–760, https://doi.org/10.1016/j.electacta.2018.02.165.

[3] T. Liebmann, C. Heubner, C. Lämmel, M. Schneider, A. Michaelis, Investigations on the effective electric loads in blended insertion electrodes for lithium-ion batteries, Chemelectrochem 6 (22) (2019) 5728–5734, https://doi.org/10.1002/celc.201901554.

[4] C. Heubner, T. Liebmann, C. Lämmel, M. Schneider, A. Michaelis, Internal dynamics of blended Li-insertion electrodes, J. Energy Storage 20 (2018) 101–108, https://doi.org/10.1016/j.est.2018.09.003.

[5] C. Heubner, T. Liebmann, C. Lämmel, M. Schneider, A. Michaelis, Synergy effects in blended electrodes for li-ion batteries: a conceptual clarification, Batter. Supercaps 5 (1) (2022) e202100171, https://doi.org/10.1002/batt.202100171.

[6] T. Liebmann, C. Heubner, M. Schneider, A. Michaelis, Understanding kinetic and thermodynamic properties of blended cathode materials for lithium-ion batteries, Mater. Today Energy 22 (2021) 100845, https://doi.org/10.1016/j.mtener.2021.100845.

[7] D. Chatzogiannakis, V. Arszelewska, P.-E. Cabelguen, F. Fauth, M. Casas-Cabanas, M.R. Palacin, Understanding charge transfer dynamics in blended positive electrodes for Li-ion batteries, Energy Storage Mater. 69 (2024) 103414, https://doi.org/10.1016/j.ensm.2024.103414.

[8] S. Jung, Mathematical model of lithium-ion batteries with blended-electrode system, J. Power Sources 264 (2014) 184–194, https://doi.org/10.1016/j.jpowsour.2014.04.072.

[9] Z. Mao, M. Farkhondeh, M. Pritzker, M. Fowler, Z. Chen, Multi-particle model for a commercial blended lithium-ion electrode, J. Electrochem. Soc. 163 (3) (2016) A458–A469, https://doi.org/10.1149/2.0321603jes.

[10] P. Albertus, J. Christensen, J. Newman, Experiments on and modeling of positive electrodes with multiple active materials for lithium-ion batteries, J. Electrochem. Soc. 156 (7) (2009) A606, https://doi.org/10.1149/1.3129656.

[11] J. Schmalstieg, C. Rahe, M. Ecker, D.U. Sauer, Full cell parameterization of a high-power lithium-ion battery for a physico-chemical model: part I. Physical and electrochemical parameters, J. Electrochem. Soc. 165 (16) (2018) A3799–A3810, https://doi.org/10.1149/2.0321816jes.

[12] M. Ecker, T.K.D. Tran, P. Dechent, S. Käbitz, A. Warnecke, D.U. Sauer, Parameterization of a physico-chemical model of a lithium-ion battery, J. Electrochem. Soc. 162 (9) (2015) A1836–A1848, https://doi.org/10.1149/2.0551509jes.

[13] Y. Ji, Y. Zhang, C.-Y. Wang, Li-Ion cell operation at low temperatures, J. Electrochem. Soc. 160 (4) (2013) A636–A649, https://doi.org/10.1149/2.047304jes.

[14] J. Costard, J. Joos, A. Schmidt, E. Ivers-Tiffée, Charge transfer parameters of Ni x Mn y Co 1− x − y cathodes evaluated by a transmission line modeling approach, Energy Technol. 9 (6) (2021) 2000866, https://doi.org/10.1002/ente.202000866.

[15] J. Euler, W. Nonnenmacher, Stromverteilung in porösen elektroden, Electrochim. Acta 2 (4) (1960) 268–286, https://doi.org/10.1016/0013-4686(60)80025-4.

[16] R. de Levie, On porous electrodes in electrolyte solutions—Iv, Electrochim. Acta 9 (9) (1964) 1231–1245, https://doi.org/10.1016/0013-4686(64)85015-5.

[17] M. Itagaki, S. Suzuki, I. Shitanda, K. Watanabe, Electrochemical impedance and complex capacitance to interpret electrochemical capacitor, Electrochemistry 75 (8) (2007) 649–655, https://doi.org/10.5796/electrochemistry.75.649.

[18] J. Illig, M. Ender, A. Weber, E. Ivers-Tiffée, Modeling graphite anodes with serial and transmission line models, J. Power Sources 282 (2015) 335–347, https://doi.org/10.1016/j.jpowsour.2015.02.038.

[19] M. Doyle, T.F. Fuller, J. Newman, Modeling of galvanostatic charge and discharge of the lithium/polymer/insertion cell, J. Electrochem. Soc. 140 (6) (1993) 1526–1533, https://doi.org/10.1149/1.2221597.

[20] K.E. Thomas, J. Newman, R.M. Darling, Mathematical modeling of lithium batteries, in: W.A. van Schalkwijk, B. Scrosati (Eds.), Advances in Lithium-Ion Batteries, 2002, pp. 345–392, https://doi.org/10.1007/0-306-47508-1_13.

[21] R. Morasch, H.A. Gasteiger, B. Suthar, Li-Ion battery active material impedance analysis I: comparison of measured NCM 111 kinetics with butler-volmer equation based predictions, J. Electrochem. Soc. 170 (8) (2023) 080522, https://doi.org/10.1149/1945-7111/acf161.

[22] E.J.F. Dickinson, A.J. Wain, The butler-volmer equation in electrochemical theory: origins, value, and practical application, J. Electroanal. Chem. 872 (114145) (2020) 1572–6657, https://doi.org/10.1016/j.jelechem.2020.114145.

[23] J. Moškon, J. Žuntar, S. Drvarič Talian, R. Dominko, M. Gaberšček, A powerful transmission line model for analysis of impedance of insertion battery cells: a case study on the NMC-Li system, J. Electrochem. Soc. 167 (14) (2020) 140539, https://doi.org/10.1149/1945-7111/abc769.

[24] Q. Zhang, Q. Guo, R.E. White, A new kinetic equation for intercalation electrodes, J. Electrochem. Soc. 153 (2) (2006) A301–A309, https://doi.org/10.1149/1.2142287.

[25] A. Latz, J. Zausch, Thermodynamic derivation of a butler–volmer model for intercalation in Li-ion batteries, Electrochim. Acta 110 (2013) 358–362, https://doi.org/10.1016/j.electacta.2013.06.043.

[26] A.M. Colclasure, R.J. Kee, Thermodynamically consistent modeling of elementary electrochemistry in lithium-ion batteries, Electrochim. Acta 55 (28) (2010) 8960–8973, https://doi.org/10.1016/j.electacta.2010.08.018.

[27] D.K. Karthikeyan, G. Sikha, R.E. White, Thermodynamic model development for lithium intercalation electrodes, J. Power Sources 185 (2) (2008) 1398–1407, https://doi.org/10.1016/j.jpowsour.2008.07.077.

[28] W. Xu, Y. Li, Y. Wang, N. Xin, K. Wang, H. Li, C. Yuan, Fabrication of nickel foam/nickel phosphide (Ni/Ni2P) composite for dendrite-free and long-life lithium metal anodes, Int. J. Electrochem. Sci. 20 (7) (2025) 101017.

[29] E. Ivers-Tiffée, A. Weber, Evaluation of electrochemical impedance spectra by the distribution of relaxation times, J. Ceram. Soc. Jpn. 125 (4) (2017) 193–201, https://doi.org/10.2109/jcersj2.16267.

[30] H. Schichlein, A.C. Müller, M. Voigts, A. Krügel, E. Ivers-Tiffée, Deconvolution of electrochemical impedance spectra for the identification of electrode reaction mechanisms in solid oxide fuel cells, J. Appl. Electrochem. 32 (2002) 875–882, https://doi.org/10.1023/A:1020599525160.

[31] M. Schönleber, D. Klotz, E. Ivers-Tiffée, A method for improving the robustness of linear kramers-kronig validity tests, Electrochim. Acta 131 (2014) 20–27, https://doi.org/10.1016/j.electacta.2014.01.034.

[32] Electrode Resistance Measurement System RM2610, HIOKI H.E.E. Corporation, 2022, pp. 1–4. https://www.hioki.com/global/download/33105.

[33] A. Lindner, S. Both, W. Menesklou, S. Hein, T. Danner, A. Latz, U. Krewer, Analyzing and improving conductive networks in commercial high-energy Ni-rich cathodes, Batter. Supercaps 7 (12) (2024) e202400503, https://doi.org/10.1002/batt.202400503.

[34] GeoDict software, release 2024 from Math2Market GmbH, Germany. https://www.geodict.com.

[35] J. Ohser, F. Mücklich, Statistical analysis of microstructures in materials science, Pract. Metallogr. 38 (9) (2000) 538–539, https://doi.org/10.1515/pm-2001-380907.

[36] A. Blumer, S. Rief, B. Planas, GeoDict 2024 user guide, MatDict handbook. Math2Market GmbH. http://doi.org/10.30423/userguide.geodict.

[37] J. Becker, A. Wiegmann, L. Cheng, B. Planas, GeoDict 2024 user guide, DiffuDict handbook. Math2Market GmbH. https://doi.org/10.30423/userguide.geodict.

[38] M. Ender, J. Joos, T. Carraro, E. Ivers-Tiffée, Quantitative characterization of LiFePO4Cathodes reconstructed by FIB/SEM tomography, J. Electrochem. Soc. 159 (7) (2012) A972–A980, https://doi.org/10.1149/2.033207jes.

[39] J. Costard, Einfluss Von Mikrostruktur Und Materialparametern Auf Die Leistungsfähigkeit Poröser Elektroden Für Lithium-Ionen Batterien, vol. 33, KIT Scientific Publishing, 2018, p. 235, https://doi.org/10.5445/ksp/1000084353.

[40] A. Mukhopadhyay, B.W. Sheldon, Deformation and stress in electrode materials for Li-ion batteries, Prog. Mater. Sci. 63 (2014) 58–116, https://doi.org/10.1016/j.pmatsci.2014.02.001.

[41] Y. Dai, L. Cai, R.E. White, Simulation and analysis of stress in a Li-ion battery with a blended LiMn 2 O 4 and LiNi 0.8 Co 0.15 Al 0.05 O 2 cathode, J. Power Sources 247 (2014) 365–376, https://doi.org/10.1016/j.jpowsour.2013.08.113.

[42] S. Gantenbein, M. Weiss, E. Ivers-Tiffée, Impedance based time-domain modeling of lithium-ion batteries: part I, J. Power Sources 379 (2018) 317–327.

[43] M.Z. Bazant, Theory of chemical kinetics and charge transfer based on nonequilibrium thermodynamics, Acc. Chem. Res. 46 (5) (2013) 1051–1238, https://doi.org/10.1021/ar300145c.

[44] J. Landesfeind, H.A. Gasteiger, Temperature and concentration dependence of the ionic transport properties of lithium-ion battery electrolytes, J. Electrochem. Soc. 166 (14) (2019) A3079–A3097, https://doi.org/10.1149/2.0571912jes.